Design Guidelines of Inductive Coils Using a Polymer Bonded Magnetic Composite for Inductive Power Transfer Systems in Electric Vehicles

Alberto Delgado, *Student Member, IEEE*, Derek Schoenberger, Jesús Ángel Oliver, *Member, IEEE*, Pedro Alou, *Member, IEEE*, and José Antonio Cobos, *Fellow, IEEE*

***Abstract*—This article studies design guidelines to optimize the inductive coils for electric vehicles by replacing the standard compact ferrite core with a compound of polymers, nanoparticles, and tile-links of ferrite and by reviewing different aspects of the winding to improve mechanical behavior and efficiency. A system composed of the studied vehicle assembly and ground assembly from the society of automotive engineers' recommended practice is defined. Fast three-dimensional (3-D) finite element simulations are performed by evaluating different geometric aspects of the vehicle assembly. In doing so, the variation of coupling factor and inductance related to the geometry can be observed and compared in order to analyze the performance when the amount of compact ferrite is reduced. The polymer bonded magnetic is, then, incorporated to improve the decreased magnetic behavior due to the reduction in ferrite. In previous works, the modeling of the litz-wire and polymer bonded magnetic were developed to accelerate the simulations. In this article, we include the modeling of the compact ferrite tile-links to further reduce the time consumption of these simulations. Moreover, simple two-dimensional simulations are described to study the windings' parasitic capacitances. The design guidelines, based on fast 3-D simulations, are detailed and validated with particular prototypes.**

***Index Terms*—Finite element analysis, finite element modeling, homogeneous model, inductive power transfer, magnetic components, wireless power transfer.**

I. Introduction

THE EMERGENCE of the electric vehicle industry has provided a wide range of possibilities for the future of transportation. Although, despite advancements within the field, the industry still faces challenges including restricted charging capabilities, high costs, and limited range. Inductive power transfer (IPT) applications are being examined in order to serve as a solution to many of these challenges by eliminating the necessity of a physical connection during the charging process. With this increase in attention on inductive power transfer applications in the electric vehicle industry [1]–[6], system efficiency and component reliability become greater areas of focus [7]–[15].

This article proposes an optimization of IPT systems in electric vehicles by conducting an analysis on the litz-wire coil design and by providing a more mechanically robust alternative to the standard compact ferrite cores traditionally used in contemporary electric vehicle applications. Using finite element simulations combined with electrical and magnetic modeling, an alternate vehicle assembly design is analyzed for IPT applications. By optimizing these areas, the proposed vehicle assembly will maintain system efficiency, increase mechanical behavior, and decrease cost of production.

Optimization of the inductive link is focused around two main components: the redesign of the litz-wire coil and the standard ferrite core. Three-dimensional (3-D) finite element simulations [16]–[18] are used to analyze the ideal thread count and layout of the wire in the vehicle assembly [19]. Additionally, an optimized core is proposed using a polymer bonded magnetic (PBM) material [18] in combination with ferrite metal tile-links in order to reduce the amount of ferrite used while maintaining the inductive link and reducing the risk of mechanical failure.

The PBM used in this article is a compound of ferrite particles. Because the PBM is designed to be flexible, in order to improve mechanical behavior, the amount of ferrite incorporated into the PBM material is limited to 50%–60%. As a result of this, the material has a relatively low conductivity and permeability compared to the compact ferrite used in standard cores. The specifications of the PBM used in this experiment are further explained in Section II.

In a previous study [20], criterion is defined in order to support the proposed designs. In this article, the design guidelines are described in detail in order to propose an inductive coil and core for the vehicle assembly. Using this apparatus, the alternate assemblies are tested and validated through comparison with the simulated results.

This article is structured into four sections. In Section II, the analytical and empirical models used to accelerate the 3-D finite element simulations are reviewed. In Section III, design guidelines for optimizing the inductive coils are presented. The guidelines are based on fast 3-D finite element simulations that

Manuscript received July 16, 2019; revised September 5, 2019 and November 4, 2019; accepted January 4, 2020. Date of publication January 8, 2020; date of current version April 22, 2020. This work was supported in part by the Ministerio de Economia, Industria y Competitividad de España under Grant DPI2016-80953-R and Grant RTC-2016-4820-4, in part by the Ferroxcube, and in part by the Elektrisola. Recommended for publication by Associate Editor J. Biela. *(Corresponding author: Alberto Delgado.)*

A. Delgado, J. Á. Oliver, P. Alou, and J. A. Cobos are with the Centro de Electrónica Industrial, Universidad Politécnica de Madrid, 28602 Madrid, Spain (e-mail: a.delgado@upm.es; jesusangel.oliver@upm.es; pedro.alou@upm.es; ja.cobos@upm.es).

D. Schoenberger is with the Mechanical Engineering and Computer Science, University of Maryland, College Park, MD 20742 USA (e-mail: dschoen1@terpmail.umd.edu).

Color versions of one or more of the figures in this article are available online at https://ieeexplore.ieee.org.

Digital Object Identifier 10.1109/TPEL.2020.2965219

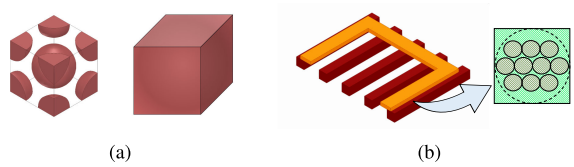

(a) (b)

Fig. 1. (a) Cubic cell of nanoparticles. (b) Winding made of litz-wire.

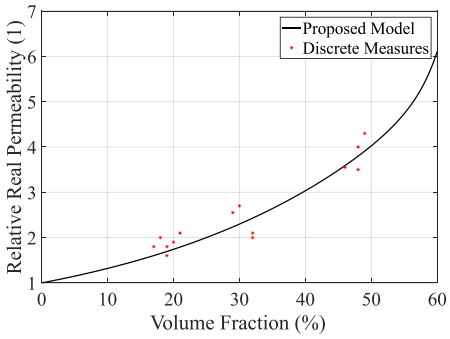

Fig. 2. Comparative results illustrating real measurement of the real permeability and the model proposed in [18] of the PBM.

can predict the magnetic and electrical properties of the inductive coil. In Section IV, based on these design guidelines, the proposed alternate designs are built, the magnetic and electrical properties are measured and compared with the simulations, and the frequency response of the inductive link is analyzed with real measurements and electrical simulations.

II. Electromagnetic Models

In this section, we review the magnetic model for the magnetic compound and litz-wire winding that were developed in [16]–[18]. The winding's magnetic losses calculation is described by analytical equations in order to obtain the parameters to perform finite element simulations. The PBM model is combined with results from ANSYS Maxwell simulations used for estimating the real relative permeability.

This article also includes the modeling of the tile-links of ferrite developed from analytical equations and the winding's parasitic capacitances from simple 2-D electrostatic finite element simulations.

A. Polymer Bonded Magnetic Modeling

The PBM is a composite of nanoparticles made from ferrite (e.g., 3C95 from Ferroxcube) embedded in a polymeric matrix. The 3-D eddy current finite element simulations of the inductive coil for this kind of material is conducted by replacing the composite with a homogeneous material [see Fig. 1(a)].

The homogeneous real permeability is analyzed and calculated in [18] as

$$\mu'_{\text{PBM}}(V_f) = e^{2.774V_f} + 4.15 \cdot 10^{-10} e^{35.69V_f} \tag{1}$$

where V_f is the volume fraction of ferrite. The measured and fitted results are compared in Fig. 2.

The imaginary part of the complex permeability can be neglected because of its small value in the low-frequency range.

B. Litz-Wire Conductors

Due to the winding's diameter and the high number of strands, using brute force simulations by finite element tools from ANSYS Maxwell is not feasible. To overcome this limitation and conduct the 3-D eddy current analysis, the actual winding is substituted for an equivalent layer [see Fig. 1(b)] that maintains the same energy and losses.

The homogeneous conductivity and complex permeability are described and calculated in [17] as

$$\sigma_l = \frac{N_{\text{turns}} N_{\text{strands}}}{2A_{el}F_s(\gamma)R_{\text{dc}}} \tag{2}$$

$$\mu''_l = \frac{2N_{\text{turns}} N_{\text{strands}} G_p(\gamma)}{\sigma\omega\mu_0 A_{el}} \tag{3}$$

$$\mu'_l = \frac{2}{\pi}\int_0^\infty \frac{\mu''_l(x)x}{x^2-\omega^2}dx + \mu'_{cte} \tag{4}$$

where γ is defined by $d/\sqrt{2}\delta$, d is the diameter of each strand, δ is the skin depth of each strand, N_{strands} is the number of strands in the litz-wire conductor, N_{turns} is the number of litz-wire conductors in the winding, R_{dc} is the dc resistance per unit length of one strand, A_{el} is the area of the equivalent layer that occupies one turn, μ'_{cte} is a value that ensures that the real permeability of the equivalent layer is 1 in low frequency and

$$F_s(\gamma) = \frac{\gamma}{4\sqrt{2}}\left[\frac{\text{ber}_0(\gamma)\text{bei}_1(\gamma) - \text{ber}_0(\gamma)\text{ber}_1(\gamma)}{\text{ber}_1^2(\gamma)+\text{bei}_1^2(\gamma)} - \frac{\text{bei}_0(\gamma)\text{ber}_1(\gamma) + \text{bei}_0(\gamma)\text{bei}_1(\gamma)}{\text{ber}_1^2(\gamma)+\text{bei}_1^2(\gamma)}\right] \tag{5}$$

$$G_p(\gamma) = -\frac{2\gamma\pi}{\sqrt{2}}\left[\frac{\text{ber}_2(\gamma)\text{ber}_1(\gamma) + \text{ber}_2(\gamma)\text{bei}_1(\gamma)}{\text{ber}_0^2(\gamma)+\text{bei}_0^2(\gamma)} + \frac{\text{bei}_2(\gamma)\text{bei}_1(\gamma) - \text{bei}_2(\gamma)\text{ber}_1(\gamma)}{\text{ber}_0^2(\gamma)+\text{bei}_0^2(\gamma)}\right] \tag{6}$$

where ber_i and bei_i are the real and imaginary part of the Kelvin functions of order i.

C. Tile-Links of Ferrite

In order to reduce the time consumption of the 3-D simulations, the analysis of the 3-D finite element simulations is conducted by considering the tile-links of ferrite, as can be seen in Fig. 3, as a homogeneous material [21], [22]. The magnetic complex permeability of the tile-links is substituted with an anisotropic complex permeability matrix that maintains the macroscopic energy and losses. The electrical conductivity is neglected.

The reluctance of one tile link can be described as

$$\Re_{\text{link}} = \frac{l_{\text{link}}}{\mu_r\mu_0 A} \tag{7}$$

where μ_r is the relative complex permeability of the ferrite, μ_0 is the vacuum permeability, A is the area of the cross section of

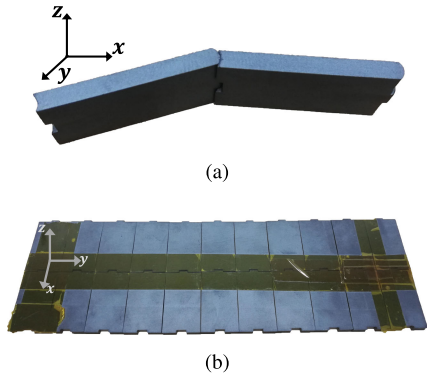

Fig. 3. (a) Two tile-links of ferrite in series. (b) Magnetic core made of 2×11 tile-links of ferrite used in one of the proposed inductive coil.

a tile link in the direction of the magnetic field and l_{link} is the length of the tile link in the direction of the field.

The work presented in [23] uses a Schwarz–Christoffel transformation to calculate the air-gap reluctance between two pieces of ferrite. The equation developed allows for the inclusion of fringing flux paths. Thus, the reluctance of the gap can be calculated as

$$\Re_{\text{gap}} = \frac{1}{\mu_0 \left[\frac{A}{l_{\text{gap}}} + \frac{2A}{e_c \pi} \left(1 + \ln \frac{l_{\text{link}} \pi}{2 l_{\text{gap}}} \right) \right]} \tag{8}$$

where e_c is the height of the tile-link.

Consequently, by using (7) and (8), the total reluctance of n tile-links in series is calculated as

$$\Re_{\text{total}} = \frac{l_{\text{total}}}{\mu_h \mu_0 A} = (n-1)\Re_{\text{gap}} + n\Re_{\text{link}}. \tag{9}$$

Then, for a core formed by n tile-links in series, the homogeneous permeability can be described by

$$\mu_h' - j\mu_h'' = \frac{l_{\text{total}}}{\mu_0 A \left((n-1)\Re_{\text{gap}} + n\Re_{\text{link}} \right)}. \tag{10}$$

The permeability matrix that describes the magnetic behavior is

$$\mu_h = \begin{bmatrix} \mu_{hx} & & \\ & \mu_{hy} & \\ & & \mu_{hz} \end{bmatrix} \tag{11}$$

where μ_{hx} and μ_{hy} are calculated with (10); and μ_{hz} is directly μ_r.

D. 2-D Electrostatic Simulation

In order to decrease the losses of the inductor, it is, therefore, important to design an inductor coil with as high of a self-resonance frequency (SRF) as possible. The SRF depends on the self-inductance, which is given, and the parasitic capacitance, which is unknown.

Based on [24], [25], three simple and fast 2-D electrostatic finite element simulations are performed. In these three simulations, the magnetic core is defined with a charge equal to zero and the shielding connected to the earth ground. The analyses are as follows.

1) Apply the differential voltage $\Delta V \neq 0$ in the winding by doing $V_1 \neq 0$ and $V_0 = 0$ [see Fig. 4(a)] in Fig. 4(d).
2) Apply the differential voltage $\Delta V = 0$ in the winding by doing $V_1 = 0$ and $V_0 \neq 0$ [see Fig. 4(b)] in Fig. 4(d).
3) Apply the differential voltage $\Delta V \neq 0$ in the winding by doing $V_1 \neq 0$ and $V_0 \neq 0$ [see Fig. 4(c)] in Fig. 4(d).

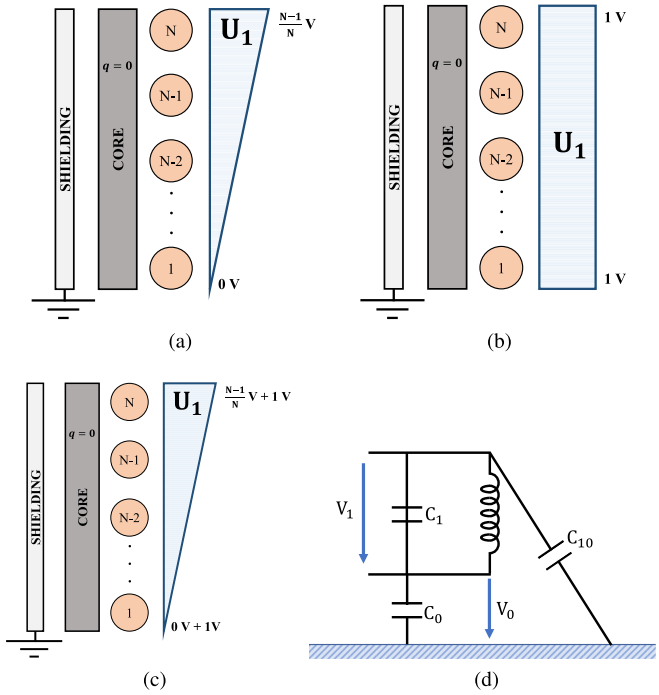

Fig. 4. Representation of finite element configuration for inductive coil.

From each simulation, the electric energy of the inductive coil is obtained. Therefore, the parasitic capacitors C_1, C_0, and C_{10} can, then, be calculated applying the previous results to the following expression:

$$E = \frac{1}{2}(C_1 + C_{10})V_1^2 + C_{10}V_1V_0 + \frac{1}{2}(C_0 + C_{10})V_0^2 \tag{12}$$

where E is the energy obtained in each case.

From this, it is straightforward to obtain the self-capacitance of the inductive coil by using

$$C_{\text{self}} = C_1 + \frac{C_{10}C_0}{C_{10} + C_0}. \tag{13}$$

III. Design Guidelines

In this section, we study the magnetic and electrical features that affect the efficiency of the inductive link in order to define a design guideline to optimize the vehicle assembly. This article will be performed using the model of the previous section, which uses finite element simulations with the ANSYS 3-D Maxwell package.

The system studied contains the ground assembly WPT1 Z1 (that is 3.7 kW and for an air-gap range of 100 to 150 mm) (see Fig. 5) from the SAE J2954 proposal [26]. The magnetic core is

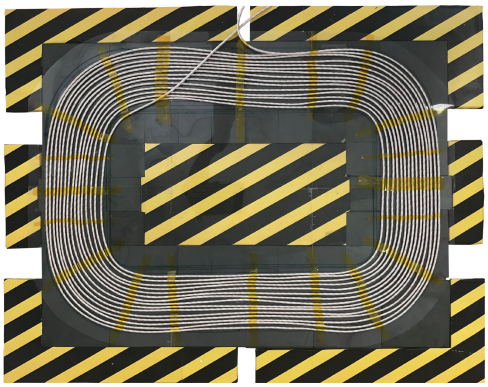

Fig. 5. Illustration of the ground assembly WPT1 and Z1 used in this article from the SAE J2954 proposal [26].

made of 3C95 from Ferroxcube [27] and the winding is made of litz-wire of 510 strands and 0.1 mm of diameter for each strand.

The dimensions of the vehicle assembly will be optimized by the proposed design guidelines. The dimensions of this coil will be set to a maximum of 350 × 350 × 30 mm. Both ground assembly and vehicle assembly have a shielding made of aluminum.

The magnetic core that is studied is made of ferrite with a real permeability of 2000 where losses are neglected.

The parameters that vary are the dimensions of the magnetic core, X_c, Y_c, Intc$_x$, and Intc$_y$, and the dimensions of the winding, X_w, Y_w, Intw$_x$, and Intw$_y$. The height of the magnetic core is adjusted to avoid saturation. This can be seen in Fig. 6(a).

To compare the results, the quality factor is assumed to be the same for all of the combinations. Then, the Figure Of Merit (F.O.M.) kL_x, where k is the coupling factor and L_x is the self-inductance of the coil designed in this article, is used to contrast the results because it is directly related with the efficiency of the inductive link that can be approximated to [20], [28], [29]

$$\eta_{\text{link}} \approx 1 - \frac{2}{kQ}. \tag{14}$$

A. Winding Design

In literature, there are different ways to optimize litz-wire [30]–[33]. In this article, we describe a practical alternative to select an optimum litz-wire construction.

In the application shown in this article, where the peak current is 22.5 A, a current density of 5 A/mm^2 is defined. Then, the total copper area needed to achieve that density can be defined as

$$A_{\text{Cu}} = \frac{A_{\text{pk}}}{J} = 4.5\,\text{mm}^2 \tag{15}$$

where A_{Cu} is the total area of copper that there is in the litz-wire, A_{pk} is the peak current that there is through the conductor, and J is the maximum density current desired.

In order to simplify the analysis, it is assumed that in litz-wire the ratio of the total copper area to the total bundle area is around 0.5. Then, if an equivalent layer is made with only one turn with a total cross section $2A_{\text{Cu}}$, where the area of copper is A_{Cu} and the number of strands is one, the equivalent layer will have the properties illustrated by the blue line shown in Fig. 7.

Then, it is possible to optimize the litz-wire by increasing the number of strands by s and the diameter of each strand is decreased with a factor $\sqrt{s}$

$$\begin{aligned} n_{\text{strands}_2} &= s \cdot n_{\text{strands}_1} \\ \varnothing_{\text{strand}_2} &= \frac{\varnothing_{\text{strand}_1}}{\sqrt{s}}. \end{aligned} \tag{16}$$

By doing so, the skin and proximity effects will be reduced. For example, let us first consider a factor of $s = 630$. The magnetic and electrical homogeneous properties are shown by the orange line in Fig. 7. One will notice that the homogeneous conductivity will be constant for higher frequencies [see Fig. 7(c)] than for one strand. As a result of this, the skin effect will be well-designed up to 2 MHz. The problem will come from the imaginary permeability [see Fig. 7(b)]. The proximity losses on the winding will be proportional to this permeability. If the optimization step is done using s = 1125 (the homogeneous properties are plotted in yellow in Fig. 7), one will notice that the skin effect will be equal, but this new s leads to the reduction of the estimated proximity effect losses by half. In the first step, the coils are evaluated using a round conductor. Once the size of the ferrite and the winding geometry are determined, these models are included in the final simulation in order to extract the ac resistance shown in Fig. 9.

To analyze the variation of the size of the winding, let us consider a magnetic core with sizes: $X_c = Y_c = 300$ mm. A set of eddy current 3-D FE simulations are performed by sweeping a) X_w and Y_w with Intw$_x$ and Intw$_y$ set to 100 mm and b) Intw$_x$ and Intw$_y$ with X_w and Y_w set to 280 mm.

Fig. 6(b) illustrates that the inductance per turn A_L will be reduced when the size of the winding is equal to the magnetic core; nevertheless, from Fig. 6(c), it is clear that the coupling factor will increase when the winding is as large as permitted (maximum size imposed). Then, from analyzing the product kL, it is understood that the size of the winding must be comparable to the magnetic core size. For this application, X_w and Y_w are selected to be 285 mm.

On the other hand, if the internal radius of the winding is analyzed, one will notice that the area not covered by the winding is directly related to the Inductance per turn A_L, as can be seen in Fig. 6(d). Since the design of the ground assembly is not symmetrical, the maximum value of the coupling factor, when Intw$_x$ and Intw$_y$ vary, will be found for each ground assembly with differing dimensions. This can be seen in Fig. 6(e). In contrast to the first case, the maximum value of the product kL is not close to the maximum value of coupling factor because the inductance decreases exponentially. In this case, the maximum value for the F.O.M. selected in this article is going to be preceded by higher values of internal radius. However, this value will depend on the number of turns that the coil requires and its distribution.

The distribution of the conductors is going to not only affect the inductance and the coupling factor, it will also influence the self-resonance of the coil, therefore increasing the ac resistance.

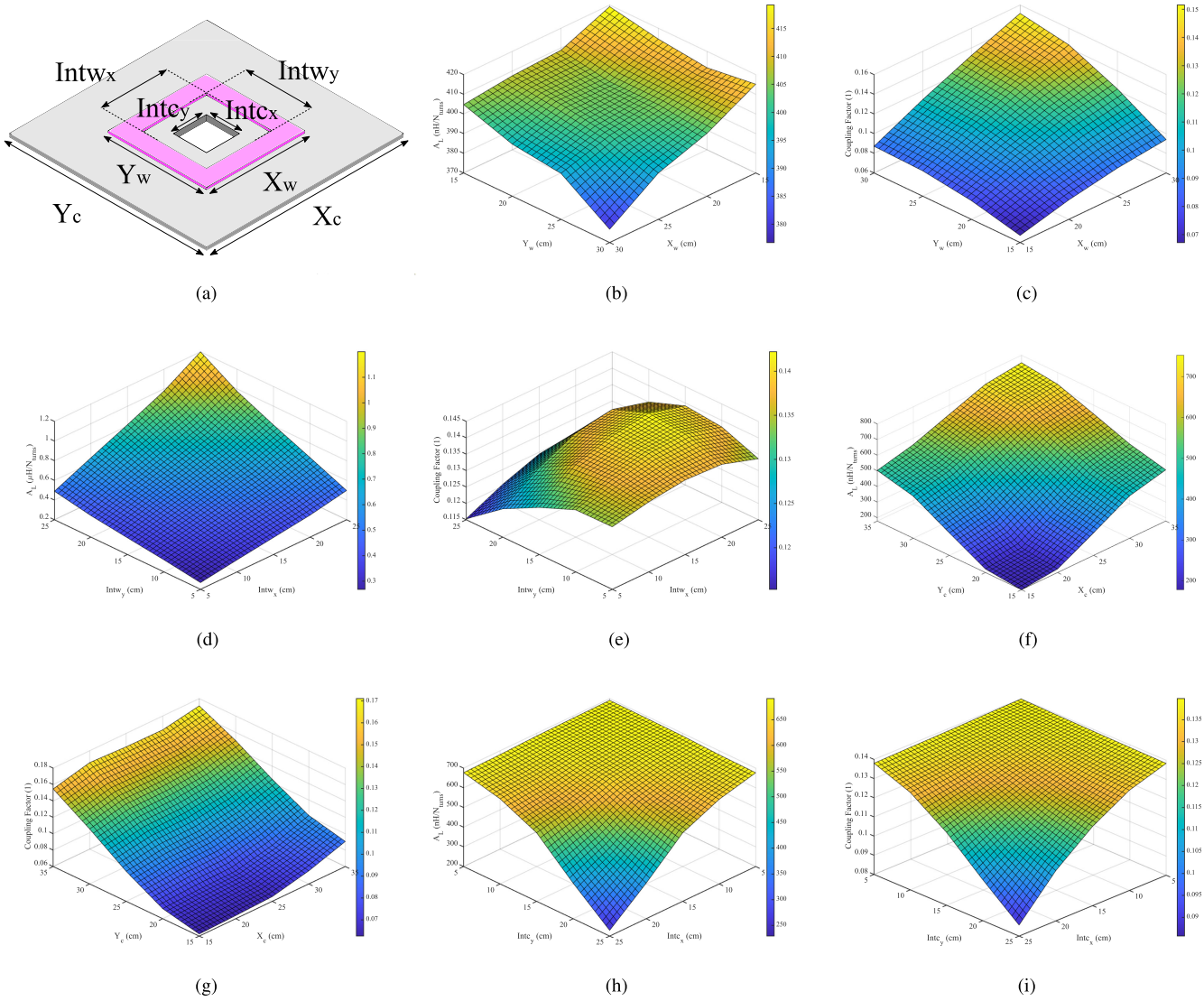

Fig. 6. (a) Geometry and parameters of the finite element model built in ANSYS Maxwell. Finite element simulation results. (b) Inductance per turn A_L of the coil due to the variation of X_w and Y_w. (c) Coupling factor of the coil due to the variation of X_w and Y_w. (d) Inductance per turn A_L of the coil due to the variation of Intw$_x$ and Intw$_y$. (e) Coupling factor of the coil due to the variation of Intw$_x$ and Intw$_y$. (f) Inductance per turn A_L of the coil due to the variation of X_c and Y_c. (g) Coupling factor of the coil due to the variation of X_c and Y_c. (h) Inductance per turn A_L of the coil due to the variation of Intc$_x$ and Intc$_y$. (i) Coupling factor of the coil due to the variation of Intc$_x$ and Intc$_y$.

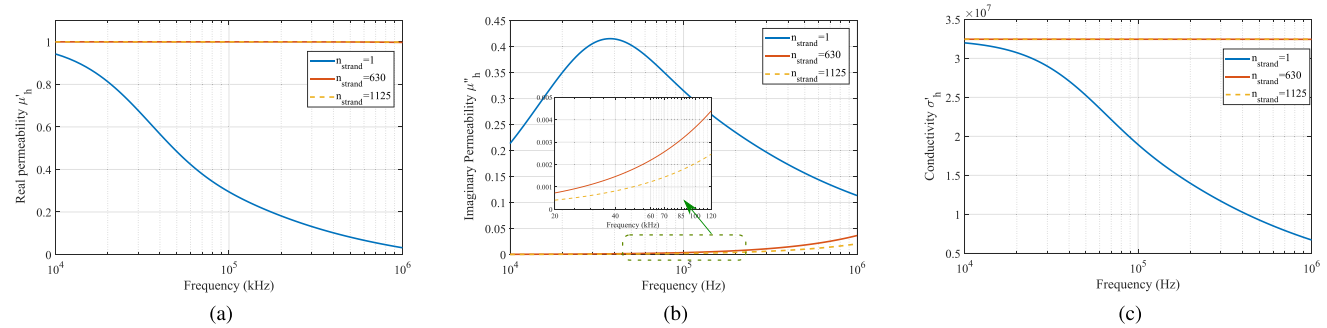

Fig. 7. Representation of the magnetic and electrical parameters of a litz-wire conductor with a copper area of A_{Cu} whose bundle occupies $A_{\mathrm{el}} = 2A_{\mathrm{Cu}}$. (a) Real part of relative permeability that is related with the energy. (b) Imaginary part of relative permeability that keeps the magnetic losses. (c) Conductivity that is related with the skin effect.

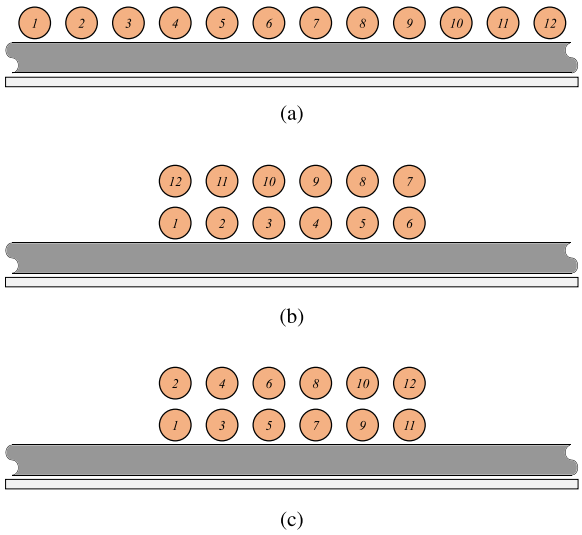

Fig. 8. Basic representation of the simple 2-D electrostatic simulation illustrating the three different litz-wire configurations examined.

TABLE I
COMPARATIVE RESULTS OF PARASITIC CAPACITANCES PER 1 M OF THE WINDING SHOWN IN FIG. 8

	C_1 (F/m)	C_{10} (F/m)	C_0 (F/m)	C_{self} (F/m)
Winding a	-1.5640e-11	7.0320e-11	8.6360e-11	2.3119e-11
Winding b	2.9680e-11	2.8960e-11	7.4480e-11	5.0532e-11
Winding c	-2.2900e-12	5.9490e-11	4.3950e-11	2.2986e-11

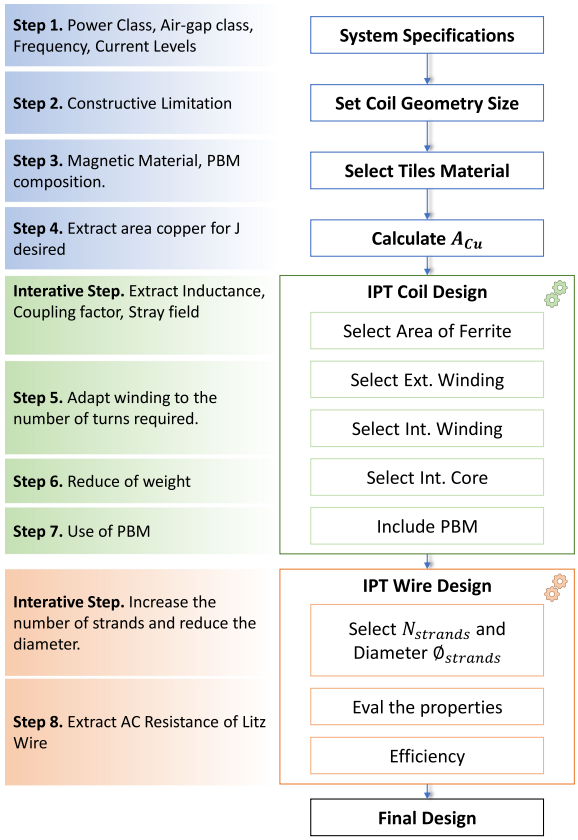

Fig. 9. Flowchart of the design guidelines proposed.

If there exists a large parasitic capacitance due to the winding manufacturer or design process, the self-resonance will appear in the lower frequency range (close to the nominal frequency of the system) and the impedance of the equivalent circuit will increase.

To illustrate the self-capacitance problems that result from the distribution of turns in the winding, three different configurations will be analyzed by simple electrostatic 2-D FE simulations.

1) All turns are positioned in series in only one layer [see Fig. 8(a)].
2) All turns are positioned in series but are distributed in two layers [see Fig. 8(b)].
3) The turns are in series but alternate layers similar to that seen in [19]. This format is shown in Fig. 8(c).

Based on the 2-D finite element analysis (see Table I), it is preferable to design the winding in two layers using the configuration shown in Fig. 8(c) because of the lower parasitic capacitance and higher self-resonance frequency compared to the other cases. In our case, a compact magnetic core is used to achieve the inductance required by the system. A 17-turn winding is constructed, where the bottom layer is made with ten turns and the top layer with seven turns, in order to comply with the specified parameters $\text{Intw}_x = \text{Intw}_y = 210$ mm defined by the combination of windings A and B. As a result of this, a self-resonance frequency of approximately 1.6 MHz is obtained. If winding C was a viable option, the self-resonance frequency would be around 2 MHz. The round conductor occupies the same space as the copper in the litz-wire and the space between the two adjacent turns is defined according to the space of the equivalent layer.

B. Magnetic Core Design

Analogous to the previous section, to study the magnetic core's size, a winding with the following parameters is considered: $X_w = Y_w = 270$ mm and $\text{Intw}_x = \text{Intw}_y = 180$ mm. The 3-D finite element simulations are, then, performed by varying a) X_c and Y_c with Intc_x and Intc_y set to 0 mm; b) Intc_x and Intc_y with X_c and Y_c set to 300 mm.

It is observed that due to the nonsymetrical design of the ground assembly, the parameter that has the most impact on the coupling factor is Y_c [see Fig. 6(g)]; nevertheless, X_c is also important to achieve higher values of inductance per turn A_L. This can be seen in Fig. 6(f). These effects are related to the winding's size. Regarding Fig. 6(f), it is observed that the inductance per turn starts to increase when the ferrite is below the winding. A similar effect can be noticed with the coupling factor. Then, it is, therefore, important to have ferrite below the winding that will increase the energy of the system. Symmetrical cores are, then, designed to range between 300 and 350 mm, where the inductance is almost constant and the coupling factor is softly increased.

With respect to the second set of simulations where the center part of the magnetic core is removed, the effect produced by the

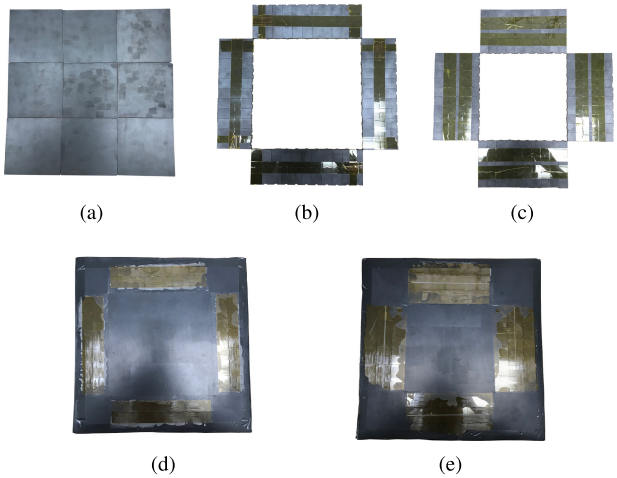

Fig. 10. Illustration of the five proposed core designs.

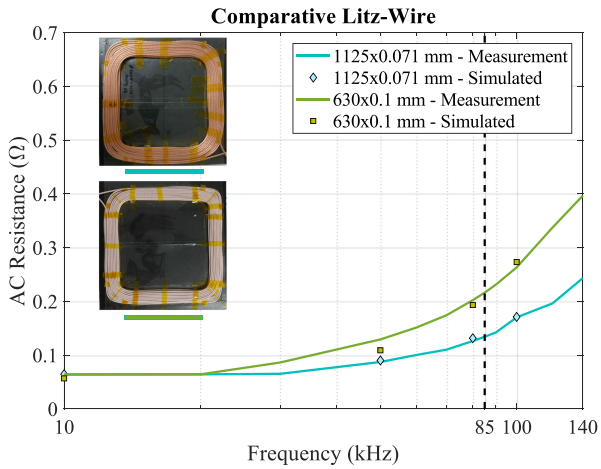

Fig. 11. Comparison of the frequency skin and proximity-effect losses (ac resistance) in a (solid line) winding with different construction: 630 strands and 1125 strands. The closed squares, that follows the green line, are the FE results of winding with 630 strands. The closed diamonds that follow the blue line, are the FE results of winding with 1125 strands.

ferrite is easily recognizable. It is possible to remove almost the whole central part of the core while maintaining the inductance per turn A_L and coupling factor. The limit can be observed in Fig. 6(h) and (i).

Consequently, five different cores will be built: 1 standard compact tiles core, 2 tile-link cores, and 2 tile-link+PBM cores as mentioned in Section II. It will be analyzed and described in the Section IV.

IV. Experimental Results

This article studies the optimization of the inductive link through redesigning two components in correspondence with the design guidelines: the conductors of the winding and the design of the magnetic core. By comparing the experimental results with these different windings and core designs, we will validate the accuracy of the simulations used to model this optimization process.

The two litz-wire coil designs are as follows. a) Litz-wire of 630 strands and 0.1 mm diameter. b) Litz-wire of 1125 strands and 0.071 mm diameter. The dimensions of each coil are 285 × 285 × 7.2 mm.

The ground assembly and state-of-the-art vehicle assembly tile-links are made of the 3C95 model from Ferroxcube.

After defining the maximum size of the inductive coil, based on the specifications (WPT1 and Z1) outlined in the proposal that this article follows, the materials of the magnetic core are selected: 3C95 from ferroxcube and PBM of 47% volume. From this, the area of copper required is known and the iterative process to obtain the coil with the required properties can begin. Based on the graphs from Fig. 6, five different cores and two different configurations of litz wire are constructed.

The five proposed core designs are as follows.

1) The state-of-the-art standard compact ferrite tile core with dimensions of 300 × 300 × 5 mm [see Fig. 10(a)].
2) A 2 × 11 ferrite tile link core that covers the four sides of the winding with each block measuring 187 × 64 × 3 mm and total dimensions of 310 × 310 × 3 mm [see Fig. 10(b)].
3) A 3 × 10 ferrite tile link core that similarly only covers the four sides of the litz-wire coil with each block measuring 170 × 96 × 3 mm and total dimension of 330 × 330 × 3 mm [see Fig. 10(c)].
4) A homogeneous PBM core, containing four 2 × 11 tile-links of ferrite, that spans an area of 320 × 320 × 3 mm [see Fig. 10(d)].
5) A homogeneous PBM core, containing four 3 × 10 tile-links of ferrite, that spans an area of 340 × 340 × 3 mm [see Fig. 10(e)].

Beginning this analysis with the comparison of the two litz-wire designs, it is observed that the homogeneous conductivity (that is related to the skin effect) is constant and equal for both configurations of litz-wire as seen in Fig. 7(c). Until 20 kHz, in the low frequency range, both windings present the same ac resistance as shown in Fig. 11 .

It is observed from 3-D finite element simulations that the 1125 threaded wire operates with approximately half as much loss at 100 kHz compared to the 630 threaded wire, see Fig. 11. It is explained by the imaginary part of the complex permeability used to model the litz-wire, shown in Fig. 7(c), that at frequencies greater than 20 kHz the imaginary permeability of the 630 litz-wire configuration becomes greater than the 1125 strand winding.

Regarding Fig. 11, the agreement of these simulated and experimental results, therefore, validates the accuracy of the 3-D finite element simulations used to model the litz-wire design.

The winding selected to study the performance of the different magnetic cores is the 1125 litz-wire.

A cost comparison [30] between the two litz-wires reveals that the 1125 threaded wire is more expensive as a result of these lower losses.

TABLE II
COMPARATIVE RESULTS OF DIFFERENT PROTOTYPES @ 100 kHz AND 100 MM. MEA = MEASUREMENT; FEA = FINITE ELEMENT ANALYSIS

	Inductance (μH)		Resistance		Q		k		η_{link}		Weight (g)
	MEA	FEA	MEA	FEA	MEA	FEA	MEA	FEA	MEA	FEA	
Standard Tiles	210	215	203	194	649	700	0.169	0.160	98.13 %	98.10 %	2079
2x11	170	180	200	186	527	609	0.130	0.132	97.31 %	97.53 %	612
3x10	185	200	208	195	558	646	0.152	0.153	97.76 %	97.93 %	840
2x11+PBM	195	193	197	187	626	651	0.150	0.153	97.86 %	97.94 %	1760
3x10+PBM	210	210	184	182	717	725	0.175	0.174	98.28 %	98.28 %	2011

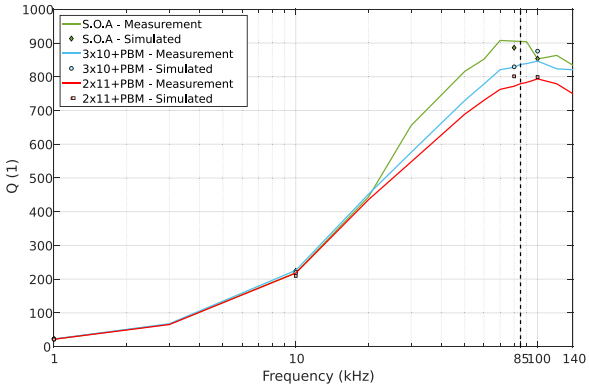

Fig. 12. Measured quality factor (solid lines) of the inductive coil compared to FE simulations (closed marks).

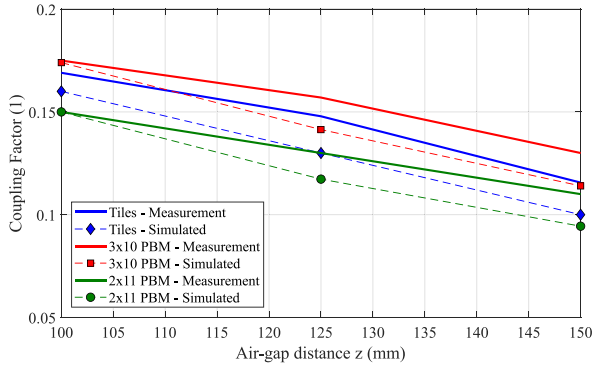

Fig. 13. Simulated and measured coupling factor with varying air-gap distance in the z-direction.

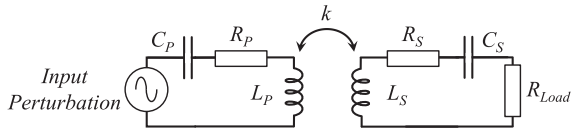

Fig. 14. Basic schematic of the setup made in order to measure the voltage gain of the system.

The magnetic and electrical parameters of the ground assembly built at 85 kHz are the following.

1) Inductance is 233 μH.
2) AC resistance is 200 mΩ.
3) Quality factor is 622.

In order to establish a basis for comparing the proposed prototypes based on the design guide described earlier in this article, the state-of-the-art standard compact ferrite core will be used with the optimized winding. The numerical simulated and measured data of this inductive coil are described in Table II. From these results, it is observed that the quality factor is greater than 600, the coupling factor is close 0.17, and the efficiency is 98.13%. The weight of the ferrite is close to 2 kg.

Considering the guidelines described in this paper, the 2×11 and 3×10 prototypes are constructed as shown in Fig. 10(b) and (c). A strong agreement is observed when comparing simulated and experimental results in Table II. As seen from this data, the inductance values for the 2×11 and 3×10 prototype cores are less than the inductance of the tiles standard core. These lower inductance values explain the decrease in quality factor and, likewise, the lower reported efficiency values. In the case of the 2×11 core, this reduction in efficiency is less than 1%, but the weight is reduced three times that of the tile core. When looking at the 3×10 prototype core, the efficiency is 0.2% less than the tiles core efficiency, but the weight is reduced by 2.5 times.

Combining these new cores with the PBM, it is noted in Table II that they present similar inductances, coupling factors, and quality factors compared to that of the standard tiles core. The quality factors (measured and simulated) of the three magnetic cores are plotted in Fig. 12. The curves present similar shape and values, which explains the similar reported efficiencies.

Additionally, one should note that the efficiency of the 3×10 PBM core being greater than the efficiency of the standard tiles core is most likely due to the $3 \times 10 +$ PBM core's 6% greater size and the higher quality factor. However, the weight of the two cores is comparable.

The simulations are supported further in Fig. 13. From these results, it is observed that the coupling factors for the three cores observed in this graph correspond with the simulated data. It is seen from the data that the 2×11+PBM core has a lower coupling factor compared to the 3×10+PBM and standard tiles cores. This lower coupling factor is likely the result of a greater decrease in volume of ferrite used. Although, despite this significant decrease in volume of ferrite in the core, the efficiency of the inductive link for each core is close in value.

From the finite element results and electrical simulations, which use a SIMetrix circuit design of the inductive link and resonant capacitors tuned at 85 kHz, an analysis is conducted of the circuit shown in Fig. 14 to obtain the frequency response and voltage gain at different loads. These results are illustrated in Fig. 15 as a comparison of the voltage gain when different cores are used.

The similarity between these graphs suggest that the frequency behavior for the three cores studied (3×10+PBM, 2×11+PBM, and standard tiles) operates independently of the inductance and coupling factor.

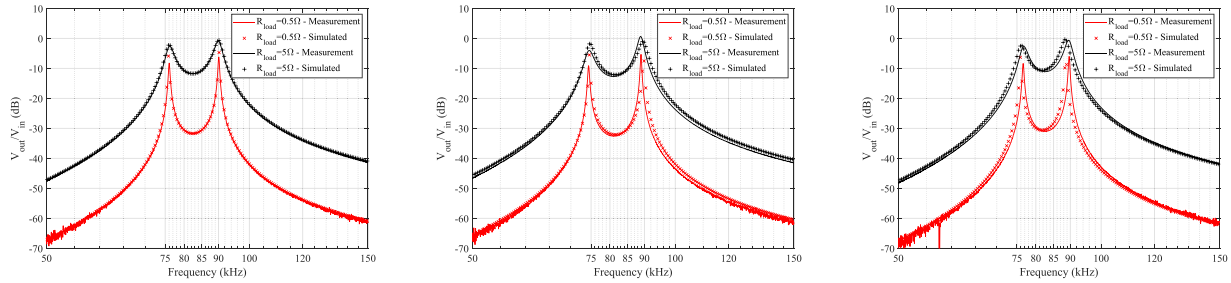

Fig. 15. Electrical circuit simulation based on the FE results using the models described compared with real measurement of the inductive link.: (a) Tiles. (b) 3 × 10+PBM. (c) 2 × 11+PBM.

V. Conclusion

In this article, the design guidelines for optimizing inductive links is outlined. In order to perform this optimization, 3-D complex finite element simulations, based on analytical models and simulations, are developed. To validate these design guidelines, different prototype cores (2 with PBM and 2 without PBM) and windings (1125 strands of 0.071 mm and 630 strands of 0.1 mm where both have the same equivalent area of copper) were constructed and analyzed against the state-of-the-art standard compact ferrite core and the simulated results. The data collected from this analysis shows that the prototypes without PBM report lower inductance and efficiency, 1% for the 2 × 11 and 0.5% for the 3 × 10, but the reduction in weight for both cores is close to 3 times less than that of the standard ferrite tile core. When combined with PBM, the prototype cores present good inductance, quality factor, coupling factor, and efficiency results, but the weight in the case of the 2 × 11 is only reduced 15% and the 3 × 10 core's weight is comparable to that of the standard tiles core. Although the weight of the prototype cores is increased by using PBM, the risk of component failure due to mechanical stress decreases significantly. Additionally, thanks to the use of ferrite tile-links, as opposed to ferrite plates, mechanical durability is further increased.

References

[1] C. Chen *et al.*, "Modeling and decoupled control of inductive power transfer to implement constant current/voltage charging and ZVS operating for electric vehicles," *IEEE Access*, vol. 6, pp. 59917–59928, 2018.

[2] M. Kim, D. Joo, and B. K. Lee, "Design and control of inductive power transfer system for electric vehicles considering wide variation of output voltage and coupling coefficient," *IEEE Trans. Power Electron.*, vol. 34, no. 2, pp. 1197–1208, Feb. 2019.

[3] O. C. Onar, M. Chinthavali, S. L. Campbell, L. E. Seiber, C. P. White, and V. P. Galigekere, "Modeling, simulation, and experimental verification of a 20-kw series-series wireless power transfer system for a toyota RAV4 electric vehicle," in *Proc. IEEE Transp. Electrific. Conf. Expo.*, Jun. 2018, pp. 874–880.

[4] C. Wang, O. H. Stielau, and G. A. Covic, "Design considerations for a contactless electric vehicle battery charger," *IEEE Trans. Ind. Electron.*, vol. 52, no. 5, pp. 1308–1314, Oct. 2005.

[5] P. Machura and Q. Li, "A critical review on wireless charging for electric vehicles," *Renewable Sustainable Energy Rev.*, vol. 104, pp. 209–234, 2019.

[6] S. Jeong, Y. J. Jang, D. Kum, and M. S. Lee, "Charging automation for electric vehicles: Is a smaller battery good for the wireless charging electric vehicles?" *IEEE Trans. Autom. Sci. Eng.*, vol. 16, no. 1, pp. 486–497, Jan. 2019.

[7] J. Deng, W. Li, T. D. Nguyen, S. Li, and C. C. Mi, "Compact and efficient bipolar coupler for wireless power chargers: Design and analysis," *IEEE Trans. Power Electron.*, vol. 30, no. 11, pp. 6130–6140, Nov. 2015.

[8] R. Tavakoli *et al.*, "Magnetizable concrete composite materials for road-embedded wireless power transfer pads," in *Proc. IEEE Energy Convers. Congr. Expo.*, 2017, pp. 4041–4048.

[9] F. Y. Lin, G. A. Covic, and J. T. Boys, "Evaluation of magnetic pad sizes and topologies for electric vehicle charging," *IEEE Trans. Power Electron.*, vol. 30, no. 11, pp. 6391–6407, Nov. 2015.

[10] M. Budhia, G. Covic, and J. Boys, "A new IPT magnetic coupler for electric vehicle charging systems," in *Proc. IEEE 36th Annu. Conf. IEEE Ind. Electron. Soc.*, 2010, pp. 2487–2492.

[11] M. Budhia, G. A. Covic, and J. T. Boys, "Design and optimization of circular magnetic structures for lumped inductive power transfer systems," *IEEE Trans. Power Electron.*, vol. 26, no. 11, pp. 3096–3108, Nov. 2011.

[12] S. Li and C. C. Mi, "Wireless power transfer for electric vehicle applications," *IEEE J. Emerg. Sel. Topics Power Electron.*, vol. 3, no. 1, pp. 4–17, Mar. 2015.

[13] C. K. T. W. Zhang, S.-C. Wong and Q. Chen, "Design for efficiency optimization and voltage controllability of series-series compensated inductive power transfer systems," *IEEE Trans. Power Electron.*, vol. 29, no. 1, pp. 191–200, Jan. 2014.

[14] J. Dai and D. C. Ludois, "A survey of wireless power transfer and a critical comparison of inductive and capacitive coupling for small gap applications," *IEEE Trans. Power Electron.*, vol. 30, no. 11, pp. 6017–6029, Nov. 2015.

[15] D. Vilathgamuwa and J. Sampath, "Wireless power transfer (WPT) for electric vehicles (EVS)—Present and future trends," in *Plug in Electric Vehicles in Smart Grids*. New York, NY, USA: Springer, 2015, pp. 33–60.

[16] A. Delgado, G. Salinas, J. A. Oliver, J. A. Cobos, J. Rodríguez, and S. Premo, "Equivalent parameters of round and litz wire conductors to obtain an equivalent layer to accelerate finite element simulations of wireless power transfer system," in *Proc. IEEE Energy Convers. Congr. Expo.*, 2018, pp. 7375–7379.

[17] A. Delgado, G. Salinas, J. A. Oliver, J. A. Cobos, and J. Rodriguez-Moreno, "Equivalent conductor layer for fast 3D finite element simulations of inductive power transfer coils," *IEEE Trans. Power Electron.*, to be published, [Online]. Available: https://ieeexplore.ieee.org/abstract/document/8882243

[18] A. Delgado, G. Salinas, J. Rodríguez, J. A. Oliver, and J. A. Cobos, "Finite element modelling of Litz wire conductors and compound magnetic materials based on magnetic nano-particles by means of equivalent homogeneous materials for wireless power transfer system," in *Proc. IEEE 19th Workshop Control Model. Power Electron.*, 2018, pp. 1–5.

[19] C. Lee, Y. Su, and S. Hui, "Multilayer stacked coreless printed spiral winding inductor with wide frequency bandwidth," in *Proc. IEEE Energy Convers. Congr. Expo.*, 2009, pp. 1002–1009.

[20] A. Delgado, J. A. Oliver, J. A. Cobos, J. Rodriguez, and A. Jiménez, "Optimized design for wireless coil for electric vehicles based on the use of magnetic nano-articles," in *Proc. IEEE Appl. Power Electron. Conf. Expo.*, 2019, pp. 1515–1520.

[21] J. Wang, H. Lin, Y. Huang, and X. Sun, "A new formulation of anisotropic equivalent conductivity in laminations," *IEEE Trans. Magn.*, vol. 47, no. 5, pp. 1378–1381, May 2011.

[22] A. Delgado, J. A. Oliver, J. A. Cobos, and J. Rodríguez, "Axisymmetric finite element modelling of compound magnetic materials based on magnetic micro-wires by means of equivalent homogeneous material," in *Proc. IEEE 18th Workshop Control Model. Power Electron.*, 2017, pp. 1–5.

[23] A. Balakrishnan, W. T. Joines, and T. G. Wilson, "Air-gap reluctance and inductance calculations for magnetic circuits using a Schwarz–Christoffel transformation," *IEEE Trans. Power Electron.*, vol. 12, no. 4, pp. 654–663, Jul. 1997.
[24] R. Asensi, R. Prieto, J. A. Cobos, and J. Uceda, "Modeling high-frequency multiwinding magnetic components using finite-element analysis," *IEEE Trans. Magn.*, vol. 43, no. 10, pp. 3840–3850, Oct. 2007.
[25] F. A. Holguín, R. Asensi, R. Prieto, and J. A. Cobos, "A simplified capacitive model for center-tapped multi-windings transformers," in *Proc. IEEE Appl. Power Electron. Conf. Expo.*, Mar. 2015, pp. 2504–2511.
[26] J. Schneider, *Wireless Power Transfer for Light-Duty Plug-in/Electric Vehicles and Alignment Methodology*, SAE Int. J2954 Taskforce, 2016.
[27] Ferroxcube, "Data sheets – soft ferrite products and accessories." Accessed: Sep. 3, 2019. [Online]. Available: www.ferroxcube.com
[28] J. C. Schuder, "Powering an artificial heart: Birth of the inductively coupled-radio frequency system in 1960," *Artif. Organs*, vol. 26, no. 11, pp. 909–915, 2002.
[29] K. Van Schuylenbergh and R. Puers, *Inductive Powering: Basic Theory and Application to Biomedical Systems*. Berlin, Germany: Springer Science & Business Media, 2009.
[30] C. R. Sullivan, "Cost-constrained selection of strand diameter and number in a litz-wire transformer winding," *IEEE Trans. Power Electron.*, vol. 16, no. 2, pp. 281–288, Mar. 2001.
[31] C. R. Sullivan and R. Y. Zhang, "Simplified design method for litz-wire," in *Proc. IEEE Appl. Power Electron. Conf. Expo.*, Mar. 2014, pp. 2667–2674.
[32] Xu Tang and C. R. Sullivan, "Optimization of stranded-wire windings and comparison with litz-wire on the basis of cost and loss," in *Proc. IEEE 35th Annu. Power Electron. Specialists Conf.*, Jun. 2004, vol. 2, pp. 854–860.
[33] C. R. Sullivan, "Optimal choice for number of strands in a Litz-wire transformer winding," in *Proc. Rec. 28th Annu. IEEE Power Electron. Specialists Conf., Formerly Power Conditioning Specialists Conf. 1970-71, Power Process. and Electron. Specialists Conf.*, Jun. 1997, vol. 1, pp. 28–35.

Alberto Delgado (Student Member, IEEE) received the B.Sc. degree in electrical engineering from the University of Málaga, Málaga, Spain, in 2016, and the M.Sc. degree in industrial electronics in 2017 from the Universidad Politécnica de Madrid, Madrid, Spain, where he is currently working toward the Ph.D. degree in industrial electronics.

During his undergraduate studies, he was awarded honors on several occasions and he achieved the Best Student of the Year Award. He was a Teaching Assistant in 2019. His research interests include modeling of dc–dc converters for inductive power transfer system, magnetic components for different applications such as RFID communications and wireless charging; and magnetic nanomaterials and micromaterials.

Derek Schoenberger is currently working toward the B.Sc. degree in mechanical engineering and computer science from the University of Maryland, College Park, MD, USA.

His research experience and interests include inductive power transfer for wireless charging, microclimate sensors for weather monitoring, and kite and wind turbine energy generation.

Jesús Ángel Oliver (Member, IEEE) received the master's and doctoral degrees in electrical engineering from the Universidad Politécnica de Madrid (UPM), Madrid, Spain, in 1996 and 2007, respectively.

He was an Assistant Professor in 2001 and Associate Professor with UPM in 2007. He has authored and coauthored more than 150 scientific papers on Journals and Conferences and he holds five patents. His research interests include modeling (dc–dc converters, magnetic components, piezoelectric transformers, fuel-cells, and dc distributed power electronic systems), fast control techniques for dc–dc converters for VRM applications and RF amplifiers, three-phase rectifiers for aircraft applications, wireless power transfer, and power systems on Chip.

Dr. Oliver has led numerous research projects with private and public funding and he has participated in more than 50 direct R&D projects with companies in Europe, US, Australia, and China. He is currently serving as an Associate Editor for the IEEE TRANSACTIONS ON POWER ELECTRONICS.

Pedro Alou (Member, IEEE) was born in Madrid, Spain, in 1970. He received the M.S. and Ph.D. degrees in electrical engineering from the Universidad Politécnica de Madrid (UPM), Madrid, Spain, in 1995 and 2004, respectively.

He is currently an Associate Professor with UPM. He has been involved in power electronics since 1995, participating in more than 50 R&D projects with the industry. He has authored or coauthored more than 100 technical papers and holds five patents. His research activity is distributed among industrial, aerospace, and military projects. His research interests include power supply systems, advanced topologies for efficient energy conversion, modeling of power electronics, advanced control techniques for high dynamic response, energy management, and new semiconductor technologies for power electronics.

José Antonio Cobos (Fellow, IEEE) received the Master's and Doctoral degrees in electrical engineering from the Technical University of Madrid (UPM), Madrid, Spain, in 1989 and 1994, respectively.

He is a Full Professor with the Universidad Politécnica de Madrid (UPM), Spain. In 2006, he was the Founder Director of the Centro de Electrónica Industrial, UPM (CEI-UPM), a university research center leading a strong industrial program in power electronics and digital systems. Since 2016, he has been the Founder President of its Industrial Council, to coordinate education and research with industry. His contributions are focused on power supply systems for industrial, aerospace, telecom, automotive, renewable energy, and medical applications. He advised more than 50 graduate students, has authored and coauthored more than 300 technical papers ($>$8000 citations, $h = 47$), and is coinventor of patents with six companies. His current research interests include energy efficiency in digital systems, RF amplifiers, renewable energy, magnetic components, transcutaneous energy transfer, and biomedical applications.

Dr. Cobos was an Adcom Member of the Power Electronics Society (IEEE-PELS) and the Chair of its Technical Committee on dc Power Supply systems. He was the General Chair of PwrSoC 2016 (IEEE-PELS and Power Supply Manufacturers Association, PSMA) and an Associate Editor for the IEEE TRANSACTIONS ON POWER ELECTRONICS and the PELS LETTERS. He conducted professional seminars and tutorials in USA, U.K., Austria, Germany, Italy, Sweden, Switzerland, Syria, Mexico, and Macedonia. He is a Steering Committee Member (Program Chair in 2019) of the IEEE Applied Power Electronics Conference. In 2016–2017, he was an RCC Fellow with Harvard University, Cambridge, MA, USA and a Fulbrighter with the University of California at Berkeley, Berkeley, CA, USA.